



Cite this: *Nanoscale*, 2019, **11**, 16837

Realizing giant tunneling electroresistance in two-dimensional graphene/BiP ferroelectric tunnel junction

Lili Kang,^{id a,b} Peng Jiang,^{id a,b} Ning Cao,^{a,b} Hua Hao,^{id a,b}
Xiaohong Zheng,^{id *a,b,c} Lei Zhang^{id *c,d} and Zhi Zeng^{a,b}

Ferroelectric tunnel junctions (FTJs) composed by sandwiching a thin ferroelectric layer between two leads have attracted great interest for their potential applications in nonvolatile memories due to the tunnel electroresistance (TER) effect. So far, almost all FTJs studied focus on adopting three dimensional (3D) ferroelectric materials as the tunnel barrier. Recently, many two-dimensional (2D) ferroelectric materials with in-plane or out-of-plane spontaneous polarization have been theoretically proposed or even fabricated, providing a new type of candidate as the tunnel barrier in FTJs. However, very little has been known about whether such 2D ferroelectric materials may lead to an excellent TER effect. In this work, using first-principles calculations, we demonstrate that a giant TER effect of around 623%, which is comparable to 3D FTJs, can be realized through the ferroelectric tunnel junction constructed with the 2D ferroelectric materials BiP and B/N-doped graphene. The analysis of the effective potential and electronic structure indicates that the large TER ratio arises from the unsymmetrical screening effects of the B/N-doped vertical van der Waals graphene/BiP leads. Our findings demonstrate the great potential of novel application of 2D ferroelectric BiP in FTJs.

Received 23rd February 2019,
Accepted 9th August 2019

DOI: 10.1039/c9nr01656b

rsc.li/nanoscale

1. Introduction

Data processing is an extremely important and rapidly developing area in the current information and digital age, and data storage plays a central role in it. Further development of data storage requires the development of a new generation of memory devices which are small, ultrafast, low energy consumption, and non-volatile. So far, the most extensively studied candidates for traditional memories are resistive random access memories (RRAMs)^{1,2} and magnetoresistive random access memories (MRAMs).^{3,4} Recently, ferroelectric tunnel junctions (FTJs), which are constructed by sandwiching a thin ferroelectric material between two leads, are also arousing great interest due to the tunneling electroresistance (TER) effect and their great potential as non-volatile memories. Here, the TER effect arises from the

switchable spontaneous polarization by an electrical field in the ferroelectric materials.

By far, the most common ferroelectric materials studied in FTJs have a three dimensional (3D) structure and especially those with a perovskite structure (ABO₃) receive the most attention.^{5–8} It is well known that the spontaneous polarization in the ferroelectric materials will lead to the charge accumulation on their surfaces. When the thickness of the ferroelectric thin film is less than a critical value, the positive and negative charges on the two surfaces will neutralize with each other. This means that, for 3D FTJs, the ferroelectricity will fade away when the thickness of the ferroelectric materials is decreased below a critical thickness. For example, a critical thickness of 24 Å has been obtained by first-principles calculations for BaTiO₃ in the SrTiO₃/BaTiO₃/SrTiO₃ junction⁹ and a critical thickness of 12 Å has been obtained experimentally for PbTiO₃.¹⁰ Such a limit in the critical thickness of the ferroelectric layer is in contradiction with the technological demand of on-going device miniaturization.

Lately, many 2D ferroelectric materials with in-plane or out-of-plane spontaneous polarization have been theoretically presented such as monolayer Group IV chalcogenides,^{11–13} III₂–VI₃ van der Waals materials,¹⁴ elemental Group V monolayer materials with buckled structure¹⁵ and even 2D perovskite oxide thin films.¹⁶ Some of them have been realized

^aKey Laboratory of Materials Physics, Institute of Solid State Physics, Chinese Academy of Sciences, Hefei 230031, China. E-mail: xhzheng@theory.issp.ac.cn

^bUniversity of Science and Technology of China, Hefei 230026, China

^cState Key Laboratory of Quantum Optics and Quantum Optics Devices, Institute of Laser Spectroscopy, Shanxi University, Taiyuan 030006, China. E-mail: zhanglei@sxu.edu.cn

^dCollaborative Innovation Center of Extreme Optics, Shanxi University, Taiyuan 030006, China

experimentally such as In_2Se_3 .¹⁷ Due to their atomic thickness, such materials should be good choices for overcoming the above critical thickness problem inherent in 3D FTJs. A more general question is, how can the in-plane or out-of-plane ferroelectricity in 2D ferroelectric materials be used for constructing high-performance FTJs? However, up to now, very little is known about whether such 2D ferroelectric materials may lead to an excellent TER effect in FTJs.¹⁸

In this work, we adopt the 2D ferroelectric Group-V compound BiP,¹⁹ which is structurally analogous to phosphorene,²⁰ as the central ferroelectric tunneling barrier and graphene/BiP vertical van der Waals (vdW) heterostructures as the left and right leads to build an all 2D FTJ. To differentiate the two leads, the graphene in the left and right leads is doped with B and N atoms, respectively. According to the study of Liu *et al.*,¹⁹ the BiP has robust in-plane ferroelectricity above room temperature and has a spontaneous polarization of $5.35 \times 10^{-10} \text{ C m}^{-1}$. By density functional theory calculations, we obtain a giant TER ratio of around 623%. It is found that the large TER ratio originates from the distinctly different screening lengths of B-doped and N-doped vertical vdW leads, satisfying a mechanism proposed by Zhuravlev *et al.*²¹

2. Structure and computation details

The structures of the graphene/BiP FTJ polarized in opposite directions (P_{\leftarrow} , P_{\rightarrow}) are presented in Fig. 1(a) and (b). Each junction consists of a 2D BiP layer extending over the whole space, covered with a graphene layer on the two sides. In our calculations, the model consists of three parts: left lead (L), right lead (R) and central (C) scattering region. The left/right leads are graphene/BiP vertical vdW heterostructures and the central region includes not only the central single BiP layer as the channel, but also part of the graphene/BiP bilayer on each side as the buffer region (see Fig. 1(b)). Since the graphene edges with dangling bonds are not stable and tend to be reconstructed,²² the graphene dangling bonds are saturated by hydrogen atoms. The system is periodic along the x direction and the transport direction is along the z axis, also the arm-

chair direction of the graphene. The rectangle unit cell size of graphene is $2.46 \text{ \AA} \times 2.46 \text{ \AA}$ while that of BiP is $4.04 \text{ \AA} \times 4.24 \text{ \AA}$. We choose the supercell size of the leads as $12.12 \text{ \AA} \times 4.24 \text{ \AA}$, which contains 5×1 graphene unit cells and 3×1 BiP unit cells, as shown in Fig. 1(c) and (d) from a top view. This way, the lattice mismatch between graphene and BiP will be less than 1.5% and the lattice constant of graphene needs to be only slightly compressed. To differentiate the two leads, the graphene layer is doped with B and N atoms, respectively, in a periodic pattern, with the doping concentration as one B or N atom in each lead supercell. The BiP channel part includes 12 unit cells. The vacuum space of 20 \AA in the y direction is used to eliminate interaction between adjacent neighbors in this direction.

Structure relaxation is performed by the Vienna *ab initio* Simulation Package (VASP),^{23,24} which is based on density functional theory (DFT) using the projector-augmented wave method and a plane wave basis set.²⁵ The generalized gradient approximation (GGA) with the form of Perdew–Burke–Ernzerhof (PBE)²⁶ is adopted for the exchange–correlation potential. The energy cutoff is set to be 500 eV. The k -point sampling grid is chosen as $4 \times 1 \times 10$. Generally, the van der Waals (vdW) interaction may reduce the interlayer distances significantly in such vdW vertical heterostructures. Thus, in the structure relaxation, the vdW interaction is taken into consideration. Structure relaxation goes on until the Hellmann–Feynman force on each atom gets below 1 meV \AA^{-1} and the total electronic energy difference between two subsequent steps gets below 10^{-6} eV .

The calculations for quantum transport are performed by the Nanocal package,²⁷ which is based on DFT combined with the non-equilibrium Green's function (NEGF) method.²⁸ The energy cutoff is set as 50 Hartree. The exchange–correlation potential adopted is GGA-PBE. The basis type is double zeta basis plus polarization (DZP) and the k -point mesh is chosen as $4 \times 1 \times 1$ for the self-consistent (SC) calculation and $50 \times 1 \times 1$ for transmission calculations. The k grid number along the transverse direction for SC calculations is reasonable considering the large lattice constant of 12.12 \AA in this direction. For transmission calculation, the k -point number needs to be much larger, thus 50 is selected in our work and the convergence is checked by adding more k points. After the NEGF-DFT self-consistent calculation of the device Hamiltonian is converged, the tunneling conductance is obtained by the Landauer formula:

$$G = \frac{2e^2}{h} \sum_{k_{\parallel}} T(k_{\parallel}, E) \quad (1)$$

where $T(k_{\parallel}, E)$ is the transmission function at energy E with $k_{\parallel} = k_x$. The TER ratio can be calculated by:

$$\text{TER} = \frac{|G_{\leftarrow} - G_{\rightarrow}|}{\min(G_{\leftarrow}, G_{\rightarrow})} \quad (2)$$

where G_{\leftarrow} and G_{\rightarrow} are the tunneling conductances of the FTJ in the P_{\leftarrow} and P_{\rightarrow} cases, respectively.

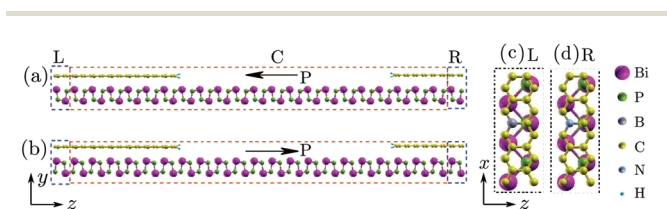


Fig. 1 Schematic plot of the FTJ: (a) for polarization pointing to left and (b) for polarization pointing to right. The structure is divided into three parts: left lead (L), right lead (R) and the central scattering region (C). The left/right leads are B/N-doped graphene/BiP vdW vertical heterostructures while the channel is the single layer 2D ferroelectric BiP. The blue dashed line box indicates one supercell in the left or right lead, while the red dashed line box indicates the central region. (c) and (d) are the top views of one supercell of the left (L) and right (R) leads shown in (a).

3. Results and discussion

First of all, the geometric and electronic properties of the FTJ are investigated. In the ferroelectric BiP, the electrical polarization points from P atoms to Bi atoms. When the polarization is reversed, each P atom will be moved from left to right or from right to left by 0.656 \AA relative to the Bi atoms in the z direction. With Heyd–Scuseria–Ernzerhof (HSE) hybrid functional calculations, we obtain the band gap as 0.918 eV , the switching barrier as 0.138 eV and the polarization as $5.226 \times 10^{-10} \text{ C m}^{-1}$, which are consistent with those reported in ref. 19, namely, 0.92 eV , 0.119 eV and $5.35 \times 10^{-10} \text{ C m}^{-1}$, respectively. The feasibility of B and N doping in graphene has also been investigated and the formation energy has been calculated. The formation energy is defined as the difference between the energies of this crystal and the stable phases of

the elements, namely, $E_{\text{form}} = \left(E_{\text{tot}} - \sum_i n_i E_i \right) / n_{\text{tot}}$, where

E_{tot} is the total energy of the supercell, n_i and E_i are the number of atoms of each constituent and its energy, and n_{tot} is the total number atoms in the supercell. For B doping, we get $E_{\text{form}} = -8.66 \text{ eV}$ per atom and for N doping, we get $E_{\text{form}} = -8.78 \text{ eV}$ per atom, which agrees well with the references²⁹ and indicates that doping B and N atoms in graphene is feasible. As a matter of fact, both B doping and N doping in graphene have been realized experimentally by a lot of ways.^{30,31} The interlayer spacing of the left and right leads is relaxed as 3.48 and 3.72 \AA , respectively. These interlayer distances hardly change with the reverse of the polarization direction. Interestingly, when the polarization direction is changed, due to the asymmetry of the electrodes, the total energy is different by 0.281 eV , with the case of left polarization smaller. The relative energy difference can be understood by a model of the interaction of a dipole \vec{P} with an external electrical field \vec{E} . Namely, the interaction energy is $\Delta\varepsilon = -\vec{P} \cdot \vec{E}$. Similarly, we can calculate the interaction energy of the electric polarization \vec{P} of the BiP layer in the field \vec{E} produced by the graphene layers. Fig. 2 shows the potential energy curve produced by a pure graphene junction with B doped in the left lead and N doped in the right lead, with the BiP ferroelectric layer artificially excluded. It is seen that an electron will have higher potential energy in the left lead than in the right lead and there is a potential difference between the left and right leads. This effectively produces an electrical field pointing from right to left. Consequently, when the ferroelectric layer is left polarized, it will have a lower energy.

Then the total transmission function of the FTJ has been calculated for both polarization directions and is presented in Fig. 3(a). Around the Fermi level, the transmission in the P_{\rightarrow} case is obviously much larger than that in the P_{\leftarrow} case. To get deeper insight into the transmission function, its k -resolved contribution has been analyzed by taking the transmission at the Fermi energy as an example. It is found that, in the first Brillouin zone, the k -points contributing most are mainly centralized around the Γ point for both polarization directions

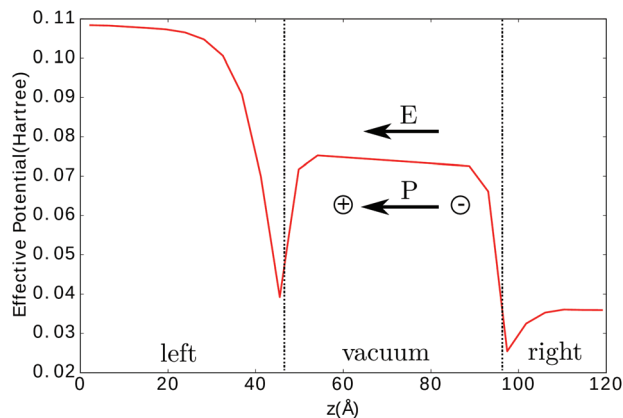


Fig. 2 The effective electrical field E produced by the graphene leads doped with B and N atoms, respectively, and the polarization of the ferroelectric layer BiP.

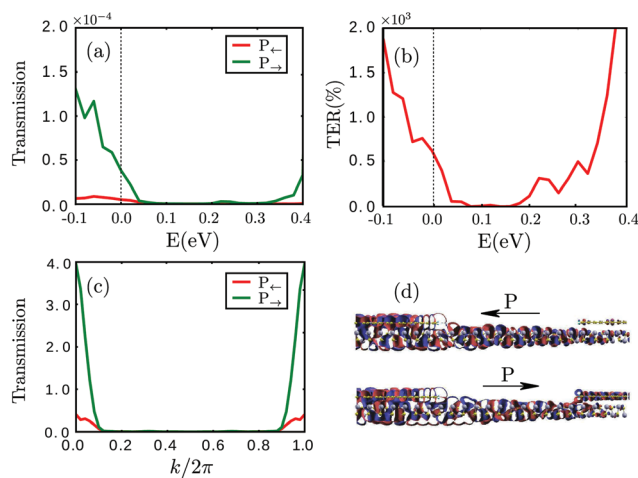


Fig. 3 (a) The transmission function for both polarization directions; (b) the TER ratio as a function of electron energy; (c) the k -resolved contribution to the transmission at the Fermi level; (d) the scattering states incoming from the left lead at $(E, k) = (0, 0)$ for both polarization directions.

(see Fig. 3(c)). Moreover, the scattering state at $E = 0$ and $k = 0$ indicates that the P_{\rightarrow} case conducts much better than the P_{\leftarrow} case, which can be seen from the much larger distribution in the right lead in the P_{\rightarrow} case, especially in the graphene layer (see Fig. 3(d)).

Having obtained the transmission function, we can get the tunneling conductance by eqn (1) and further the TER ratio by eqn (2). The TER as a function of electron energy is shown in Fig. 3(b), from which we see that the maximum TER reaches the order of 1000%. The analysis for TER at E_F is more interesting. The conductance in the P_{\leftarrow} case is $G_{\leftarrow} = 5.253 \times 10^{-6} G_0$ ($G_0 = 2e^2/h$: the conductance quantum) and increases to $G_{\rightarrow} = 3.803 \times 10^{-5} G_0$ when the direction of polarization is reversed. Therefore, we obtain a giant TER ratio $R = 623\%$, which is comparable to the TER ratio calculated in the 3D FTJs.^{5,32}

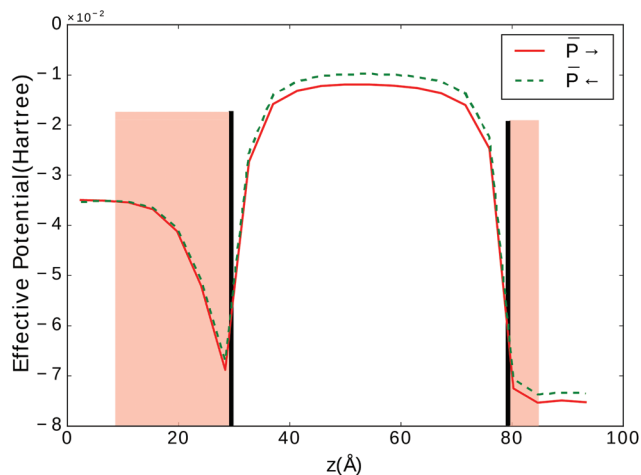


Fig. 4 The macroscopic averaged effective potential (\bar{P}_σ) along the z direction for both polarization directions ($\sigma = \leftarrow, \rightarrow$). The shadowed areas in the leads where the effective potential is more than 1% deviated from the lead bulk value roughly indicate the screening lengths of the two leads. The bold vertical lines indicate the interfacial positions.

It is well known that for a FTJ with a large TER ratio, it should have either unsymmetrical leads or unsymmetrical interfaces. In our study, we dope B atoms in the graphene layer of the left lead and N atoms in the right lead to achieve unsymmetrical leads. Such leads generally result in different potential barriers when the polarization is reversed. To confirm this, for both the P_\rightarrow and P_\leftarrow cases, the effective potential of the system, which is the sum of the Hartree potential and the exchange–correlation potential, is averaged in the xy plane for each z position and further the macroscopic averaged potential is calculated by averaging the above effective potential over a period of the BiP lattice along the z direction. The macroscopic averaged potentials for the two polarization directions are shown in Fig. 4. It is shown that the potential barrier in the P_\leftarrow case is overall higher than that in the P_\rightarrow case, which leads to marked difference in the equilibrium conductance, namely, $G_\leftarrow \ll G_\rightarrow$.

It is more interesting to note the difference in the potential at the left and right interfaces. It is known that for a nanoscale or molecular device with a central region connected to two infinite leads, the potential changes very abruptly at the interface but saturates gradually to the bulk value when it goes deep into the leads. This is clearly seen in Fig. 4. However, it saturates much more slowly at the left interface than that at the right interface, which means the screening length of the left lead is much longer than that of the right lead. From this, we can well understand the difference in the potential barriers in the two opposite polarization directions by a classical model.

Based on earlier studies,²¹ for leads with significantly different screening lengths, the conductance can change by a few orders of magnitude reflecting the different potential profile seen by transport electrons for the two opposite polarization directions. We can analyze the process as shown in

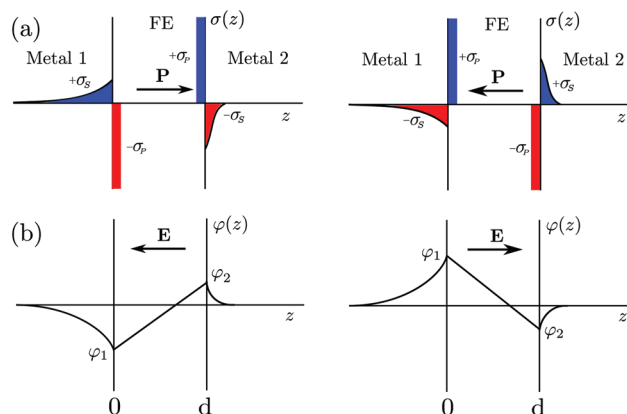


Fig. 5 Electrostatics of the FTJ for polarization (P) pointing to the right and left: (a) the charge distribution and (b) the corresponding electrostatic potential profile. ‘ E ’ stands for electrical field. The screening length of the left lead is supposed to be longer than that of the right lead ($\delta_L > \delta_R$).

Fig. 5. In the figure σ_P indicates the polarization charge because of the spontaneous polarization field inside the ferroelectric materials and σ_S is the screening charge induced by leads. d is the tunneling barrier width. Here, the screening length of the left lead is supposed to be longer than the right lead ($\delta_L > \delta_R$), exactly as in the case of our study. The σ_S at the two interfaces are equal because of the charge conservation condition. The charge distributions for the two polarization directions are presented in Fig. 5(a). According to the Thomas–Fermi model of screening,^{21,33,34} the screening potential can be written as:

$$\varphi(z) = \begin{cases} \frac{\sigma_S \delta_L e^{-|z|/\delta_L}}{\epsilon_0} & z \leq 0 \\ -\frac{\sigma_S \delta_R e^{-|z-d|/\delta_R}}{\epsilon_0} & z \geq d \end{cases} \quad \text{for } P_\leftarrow \quad (3)$$

$$\varphi(z) = \begin{cases} -\frac{\sigma_S \delta_L e^{-|z|/\delta_L}}{\epsilon_0} & z \leq 0 \\ \frac{\sigma_S \delta_R e^{-|z-d|/\delta_R}}{\epsilon_0} & z \geq d \end{cases} \quad \text{for } P_\rightarrow. \quad (4)$$

We see that the potential at the left and right interfaces is asymmetric because of the asymmetric screening length of the two leads (see Fig. 5(b)). Further, when the polarization is reversed, the potential barrier height for tunneling electrons to experience is much different in the two kinds of polarizations. This is the reason why the conductance can change by a few orders of magnitude for the two opposite polarization directions. Therefore, we need to break the symmetry of the left and right leads for getting the asymmetric screening lengths of the two leads. In fact, the earliest study about 3D FTJs used two different metals as the leads. For example, the screening length of the Au lead was 0.6 Å, while the screening length of the Bi lead was 6.5 Å.³³ And generally, metallic leads have much shorter screening lengths than semiconducting leads. In our study, the different screening lengths are achieved by

doping B atoms in the left lead and N atoms in the right lead, which results in $\delta_L \sim 20 \text{ \AA}$ and $\delta_R \sim 5 \text{ \AA}$, as marked by the shadowed areas in Fig. 4.

We wondered what causes the distinctly different screening lengths. To solve this puzzle, we investigated the electronic structures of the left and right leads. Without loss of generality, we only demonstrate the P_{-} case. The band structures of the left (B-doping) and right (N-doping) leads are given in Fig. 6(b) and (c). As a contrast, the band structure of the undoped graphene/BiP structure has also been given (see Fig. 6(a)). From Fig. 6(a), the Dirac point of graphene is still observable but a very small number of electrons transfer from the BiP layer to the graphene layer, indicated by the filling above the Dirac point of the graphene bands and unfilling of the valence band maximum of the BiP band along the G - X line. After doping B or N atoms, the Dirac point of the graphene layer is missing due to the strong hybridization of B/N atoms and C atoms. It is apparent that the left lead is p-type doping and the right lead is n-type doping since B atoms introduce holes which further get electrons from the semiconducting BiP layer while N atoms donate electrons to fill the conduction bands of graphene. However, a great difference can be observed in the two leads. In Fig. 6(b), in some regions of the first Brillouin zone of the left lead (see Fig. 6(b)), such as along the G - X , S - Y and G - S directions, there are large gaps slightly above the Fermi level, while such gaps are absent in the right lead (see Fig. 6(c)). Moreover, the bands crossing the Fermi level along these directions are more dispersive and the band

widths are much larger in the right lead. These facts indicate that the left lead is much more 'semiconducting' than the right lead, which partly reflects why the screening length of the left lead is larger than that of the right lead. From another point of view, and more straightforwardly, each B-doped supercell in the left lead has two electrons less than the N-doped supercell in the right lead, which results in smaller electron density in the left lead. To be specific, it is $2.705 \times 10^{16} \text{ cm}^{-2}$ in the left lead and $2.744 \times 10^{16} \text{ cm}^{-2}$ in the right lead. Since smaller average electron density gives rise to a weaker screening effect,³³ a longer screening length is obtained in the left lead. Actually, in a more simple system with the BiP layer artificially removed, as seen in Fig. 2, the screening length of B-doped graphene (left lead) is also much larger than that in the N-doped graphene (right lead), with similar behavior in the BiP/graphene hybrid system. Thus, the different screening lengths are mainly determined by the differently doped graphene layers.

Finally, we have more discussion on the interaction between the graphene layer and the BiP layer. From the projected density of states (PDOS) shown in Fig. 6(d), we find that the states at the Fermi level of the left lead are contributed by P, Bi, C and B atoms. In contrast, the states at the Fermi level of the right lead are contributed only by C and N atoms. This can be understood by the differential charge density shown in Fig. 6(f) and (g). From Fig. 6(f), it is obvious that the electrons transfer from the BiP layer to the graphene layer since B atoms introduce holes that receive electrons from the BiP layer,

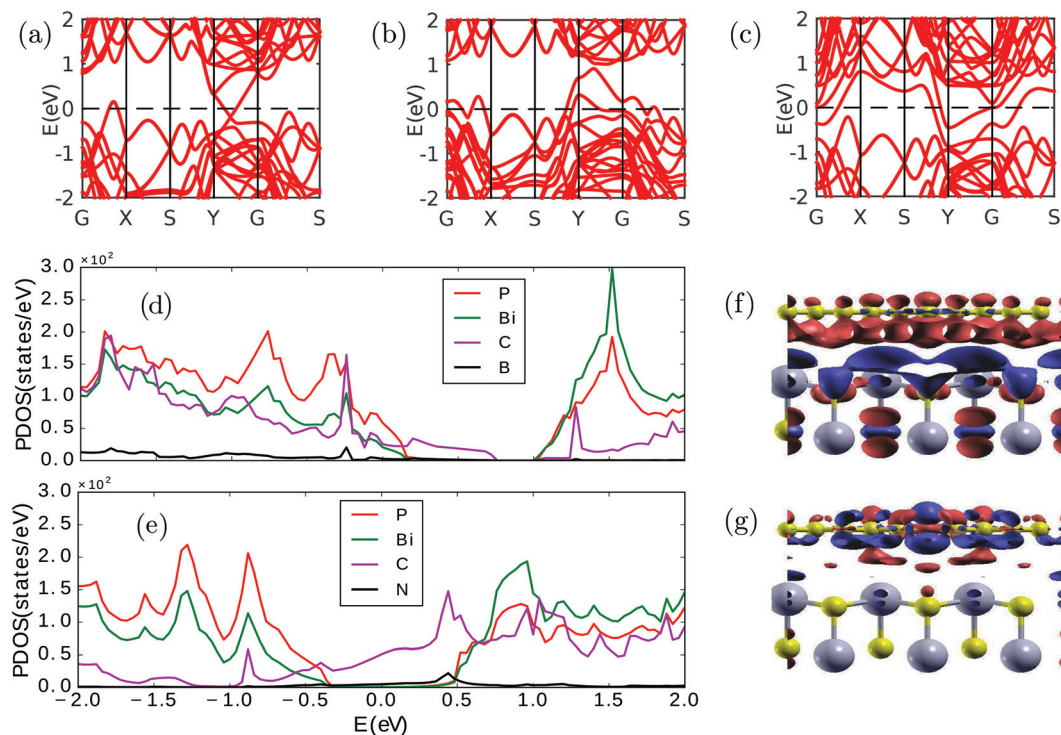


Fig. 6 The band structure of: (a) the un-doped graphene/BiP structure; (b) the B-doped graphene/BiP (left lead); (c) the N-doped graphene/BiP (right lead). (d) and (e) are the PDOS of the left and right leads. (f) and (g) are the deformation charge density of the left and right leads, respectively, where the red region denotes the electron accumulation area while the blue region denotes the electron depletion area.

which makes the valence bands of the BiP layer partially filled. However, there is no charge transfer between BiP and graphene layers, thus all the valence bands of BiP are fully filled in the right lead and the Fermi level is right inside the BiP gap. The full filling of the BiP valence bands in the right lead can also be understood as follows. In the undoped BiP/graphene system (see Fig. 6(a)), there is some electron transfer from BiP to graphene. After N doping in graphene, electrons donated by the N atoms drive some electrons back to the BiP layer, making it neutral. From this, we see another clear difference between the B-doped and N-doped leads.

4. Conclusion

In conclusion, we have designed a 2D FTJ from 2D ferroelectric material BiP and graphene, with a single layer of BiP as the central ferroelectric tunneling barrier and graphene/BiP van der Waals vertical heterostructures as the leads. By means of B/N doping in the graphene layers of the left/right leads to break the symmetry of the left and right leads, we get asymmetric screening lengths in the two leads. It is well known that when the concept of the giant electroresistance (GER) effect in ferroelectric tunnel junctions was first proposed,²¹ the mechanism demanded asymmetric leads with different screening lengths. The role of the ferroelectric tunnel barrier lies in the fact that when the polarization is reversed, the average tunnel barrier height will be changed. The change in the tunnel barrier results in different transmission. In this FTJ, we obtain a giant TER ratio of around 623%, which is comparable to 3D FTJs. Electronic structure calculations indicate that the different screening lengths arise from the different semiconducting features and electron density in the B and N doped vdW vertical heterostructures. These findings demonstrate the great potential of 2D ferroelectric materials in FTJs and may initiate further experimental interests in them.

Conflicts of interest

There are no conflicts to declare.

Acknowledgements

We gratefully acknowledge financial support by the National Natural Science Foundation of China under Grant No. 11574318 (X. Z.), 11974355 (X. Z.), and 11704232 (L. Z.); Shanxi Science and Technology Department (No. 201701D121003) (L. Z.) and the Program of State Key Laboratory of Quantum Optics and Quantum Optics Devices (No: KF201810) (X. Z. and L. Z.); National Key R&D Program of China under Grant No. 2017YFA0304203 (L. Z.); Shanxi Province 100-Plan Talent Program (L. Z.). Calculations were performed in the Center for Computational Science of CASHIPS, the ScGrid of the Supercomputing Center and

Computer Network Information Center of Chinese Academy of Sciences.

References

- 1 A. Sawa, *Mater. Today*, 2008, **11**, 28–36.
- 2 D. B. Strukov, G. S. Snider, D. R. Stewart and R. S. Williams, *Nature*, 2008, **453**, 80.
- 3 Y.-Q. Ke, K. Xia and H. Guo, *Phys. Rev. Lett.*, 2008, **100**, 166805.
- 4 Y.-Q. Ke, K. Xia and H. Guo, *Phys. Rev. Lett.*, 2010, **105**, 236801.
- 5 L.-L. Tao and J. Wang, *Appl. Phys. Lett.*, 2016, **108**, 062903.
- 6 K. Klyukin, L.-L. Tao, E. Y. Tsymbal and V. Alexandrov, *Phys. Rev. Lett.*, 2018, **121**, 056601.
- 7 P.-Z. Wang, T.-Y. Cai, S. Ju and Y.-Z. Wu, *Sci. Rep.*, 2016, **6**, 24209.
- 8 Z. Wen, C. Li, D. Wu, A. Li and N. Ming, *Nat. Mater.*, 2013, **12**, 617.
- 9 J. Junquera and P. Ghosez, *Nature*, 2003, **422**, 506.
- 10 D. D. Fong, G. B. Stephenson, S. K. Streiffer, J. A. Eastman, O. Auciello, P. H. Fuoss and C. Thompson, *Science*, 2004, **304**, 1650–1653.
- 11 F. Xiong, X. Zhang, Z. Lin and Y. Chen, *J. Materiomics*, 2018, **4**, 139–143.
- 12 A. I. Lebedev, *J. Appl. Phys.*, 2018, **124**, 164302.
- 13 R. Fei, W. Kang and L. Yang, *Phys. Rev. Lett.*, 2016, **117**, 097601.
- 14 W.-J. Ding, J.-B. Zhu, Z. Wang, Y.-F. Gao, D. Xiao, Y. Gu, Z.-Y. Zhang and W.-G. Zhu, *Nat. Commun.*, 2017, **8**, 14956.
- 15 C.-C. Xiao, F. Wang, S.-Y. A. Yang, Y.-H. Lu, Y.-P. Feng and S.-B. Zhang, *Adv. Funct. Mater.*, 2018, **28**, 1707383.
- 16 J.-L. Lu, W. Luo, J.-S. Feng and H.-J. Xiang, *Nano Lett.*, 2018, **18**, 595–601.
- 17 C.-J. Cui, W. J. Hu, X.-X. Yan, C. Addiego, W.-P. Gao, Y. Wang, Z. Wang, L. Li, Y.-C. Cheng, P. Li, *et al.*, *Nano Lett.*, 2018, **18**, 1253–1258.
- 18 X.-W. Shen, Y.-W. Fang, B.-B. Tian and C.-G. Duan, *ACS Appl. Electron. Mater.*, 2019, **1**, 1133–1140.
- 19 C. Liu, W.-H. Wan, J. Ma, W. Guo and Y.-G. Yao, *Nanoscale*, 2018, **10**, 7984–7990.
- 20 J. Qiao, X. Kong, Z. X. Hu, F. Yang and W. Ji, *Nat. Commun.*, 2014, **5**, 4475.
- 21 M. Y. Zhuravlev, R. F. Sabirianov, S. Jaswal and E. Y. Tsymbal, *Phys. Rev. Lett.*, 2005, **94**, 246802.
- 22 L. L. Song, X. H. Zheng, R. L. Wang and Z. Zeng, *J. Phys. Chem. C*, 2010, **114**, 12145–12150.
- 23 G. Kresse and J. Furthmüller, *Phys. Rev. B: Condens. Matter Mater. Phys.*, 1996, **54**, 11169.
- 24 G. Kresse and D. Joubert, *Phys. Rev. B: Condens. Matter Mater. Phys.*, 1999, **59**, 1758.
- 25 P. E. Blöchl, *Phys. Rev. B: Condens. Matter Mater. Phys.*, 1994, **50**, 17953.
- 26 J. P. Perdew, K. Burke and M. Ernzerhof, *Phys. Rev. Lett.*, 1996, **77**, 3865.

- 27 J. Maassen, M. Harb, V. Michaud-Rioux, Y. Zhu and H. Guo, *Proc. IEEE*, 2013, **101**, 518–530.
- 28 J. Taylor, H. Guo and J. Wang, *Phys. Rev. B: Condens. Matter Mater. Phys.*, 2001, **63**, 245407.
- 29 P. Rania and V. K. Jindal, *RSC Adv.*, 2013, **3**, 802–812.
- 30 S. Agnoli and M. Favaro, *J. Mater. Chem. A*, 2016, **4**, 5002–5025.
- 31 H. Wang, T. Maiyalagan and X. Wang, *ACS Catal.*, 2012, **2**, 781–794.
- 32 L.-L. Tao and J. Wang, *J. Appl. Phys.*, 2016, **119**, 224104.
- 33 R. Mehta, B. Silverman and J. Jacobs, *J. Appl. Phys.*, 1973, **44**, 3379–3385.
- 34 N. W. Ashcroft and N. D. Mermin, *Solid State Physics*, Saunders College Publishing, New York, Holt, Rinehart and Winston, 1976.